Thermoelectric porous laser-induced graphene-based strain-temperature decoupling and self-powered sensing

Li Yang [1,2] ✉, Xue Chen[3], Ankan Dutta[4], Hui Zhang[2,3], Zihan Wang[5], Mingyang Xin[1], Shuaijie Du[3], Guizhi Xu[2,3] & Huanyu Cheng [4] ✉

Despite rapid developments of wearable self-powered sensors, it is still elusive to decouple the simultaneously applied multiple input signals. Herein, we report the design and demonstration of stretchable thermoelectric porous graphene foam-based materials via facile laser scribing for self-powered decoupled strain and temperature sensing. The resulting sensor can accurately detect temperature with a resolution of 0.5°C and strain with a gauge factor of 1401.5. The design of the nanocomposites also explores the synergistic effect between the porous graphene and thermoelectric components to greatly enhance the Seebeck coefficient by almost four times (from 9.703 to 37.33 µV/°C). Combined with the stretchability of 45%, the self-powered sensor platform allows for early fire detection in remote settings and accurate and decoupled monitoring of temperature and strain during the wound healing process in situ. The design concepts from this study could also be leveraged to prepare multimodal sensors with decoupled sensing capability for accurate multi-parameter detection towards health monitoring.

Wearable sensors with flexibility[1], portability[2], high sensitivity[3], and biocompatibility[4] have been widely used in health monitoring[5–7], preventive medicine[8,9], disease diagnosis[10–12], and human-machine interactions[13–15], among others[16,17]. However, the use of external batteries (with matching circuits) for electrical supply creates challenges in device miniaturization. Efforts to address this challenge have led to the exploration of integrated powering components[18–21] such as battery arrays and supercapacitors[22] or of energy harvesting units (e.g., photovoltaic[23], triboelectric[24–28], thermoelectric[29–31], piezoelectric[32–34], and biological reactions[35,36]). The ubiquitous temperature gradients in nature can generate potential differences through the selective migration of electrons by leveraging the Seebeck effect[37–39]. Capable of producing stable and continuous voltage from a temperature gradient, high-performance thermoelectric energy harvesting based on stretchable materials is promising for wearable electronics[40–44]. Representative

efforts include a flexible dual-parameter pressure-temperature sensor based on a three-dimensional spiral textured thermoelectric bismuth telluride (Bi_2Te_3) film[45]. With a maximum Seebeck coefficient of -181 µV K^{-1}, the device detects temperature with a high sensitivity of 123.2 µV K^{-1} leg^{-1} and fast response of 0.5 s, along with a pressure sensitivity of 120 Pa^{-1}. Connecting silver nanowire-based soft electrodes to Bi_2Te_3-based thermoelectric legs yields a compliant thermoelectric generator, which allows adaptation to curved surfaces[46]. Magnetic self-assembled metal particles in the elastomeric substrate form soft thermal conductors to significantly enhance heat transfer to the thermoelectric legs, thereby maximizing the energy conversion efficiency.

On the other hand, the porous laser-induced graphene (LIG) foams exhibit compelling advantages for high-performance sensing[47], including one-step patterning preparation[48], a high specific surface area[49], and superior conductivity[50]. Although the porous LIG holds great promise

[1]School of Health Sciences and Biomedical Engineering, Hebei University of Technology, 300130 Tianjin, China. [2]State Key Laboratory of Reliability and Intelligence of Electrical Equipment, Hebei University of Technology, 300130 Tianjin, China. [3]School of Electrical Engineering, Hebei University of Technology, 300130 Tianjin, China. [4]Department of Engineering Science and Mechanics, The Pennsylvania State University, University Park, Pennsylvania 16802, USA. [5]School of Mechanical Engineering, Hebei University of Technology, 300401 Tianjin, China. ✉e-mail: yangli5781@126.com; huanyu.cheng@psu.edu

for multi-parameter sensing, the accurate detection of simultaneously applied input signals is still challenging. By mimicking the human skin, wearable sensors are developed to simultaneously monitor and decouple multiple physical stimuli (e.g., strain-temperature[29]) without interference[51]. The design often relies on the exploration of assembled sensor arrays through either in-plane (tiling) or out-of-plane (lamination) methods with distinct sensing functions in each sensor[52]. Compared with sensing arrays, a single sensing unit with multiple sensing mechanisms could reduce the complexity and the cost[53,54]. As a representative example, stretchable thermoelectric materials can simultaneously and accurately detect temperature and pressure from the measured two independent electrical signal outputs[51,55]. However, it is still a great challenge to fabricate a low-cost, self-powered, dual-parameter high-performance sensor for decoupled signal detection.

This study reports the design, evaluation, and application of a thermoelectric 3D porous laser-induced graphene foam with a simple low-cost laser direct writing technique. Combined with the pre-strain strategy and high-performance thermoelectric component, Poly (3,4-ethylenedioxythiophene)/poly (styrenesulfonate) (PEDOT:PSS), the stretchable thermoelectric 3D porous graphene foam nanocomposites can be created for decoupled and self-powered sensing. The significant π electrons in the porous graphene engage in π-π conjugation within PEDOT:PSS to modify the arrangement of polymer chains within the PEDOT:PSS matrix for improved Seebeck coefficient and boosted thermoelectric properties. The measured resistance and voltage from the thermoelectric porous graphene foam-based materials provide the decoupled detection of strain (with a maximum Gauge factor of 1401.5) and temperature (with a resolution of 0.5°C), respectively. Taken together with the stretchability of 45%, the resulting self-powered and decoupled sensors provide unique application opportunities from wound healing monitoring in vivo to a self-powered fire alarm in remote settings.

Results

Fabrication of porous graphene foam-based materials

The fabrication of the porous graphene foam-based materials starts with laser direct writing of carbon-containing materials, such as commercial polyimide (PI) films, to create patterned porous graphene sensors (Fig. 1a). Infiltrating elastomer such as polydimethylsiloxane (PDMS) precursor into the porous graphene foams followed by curing peels them from the PI to result in a stretchable porous graphene foam on PDMS with a thickness of ca. 300 µm. The porous 3D graphene foam with a large number of randomly stacked 2D graphene flakes is highly sensitive to strain and exhibits good thermoelectric properties to respond to temperature differences. The resulting stretchable thermoelectric graphene foams-based materials driven by the temperature differential between the surrounding and the skin (Fig. 1b) provide self-powered and decoupled sensing of temperature and strain for in situ wound healing monitoring and remote fire alarm warning (Fig. 1b–d).

Characterization of porous graphene foams

Scanning electron microscopy (SEM) images of the porous graphene foams reveal the infiltration of PDMS in the porous structure with mesopores (~2 µm) (Supplementary Fig. 1a) and interconnected 3D structures (thickness about 20 µm) (Supplementary Fig. 1b). The Raman spectra exhibit three characteristic peaks: the G peak (1580 cm^{-1}), the D peak (1330 cm^{-1}), and the 2D peak (2900 cm^{-1}) (Supplementary Fig. 1c). The presence of few-layered graphene and a large number of defects are confirmed by a relatively large ratio I_D/I_G of 0.70 as in the literature[56]. The presence of C, O, and Si, along with the absence of N, from the high-resolution XPS spectra reveals the chemical composition of the composite (Supplementary Fig. 1d).

Performance characterizations of the porous graphene foam to the temperature gradient and tensile strain

A thermal gradient (ΔT) established across the stretchable composite film by two parallel-connected Peltier thermoelectric modules (one heater and one cooler) characterizes its thermoelectric properties (Fig. 2a). As the temperature gradient increases, the current-voltage (I–V) curves are shifted with increased x-intercept from the generated thermoelectric potential and almost unchanged slope (Fig. 2b). The thermoelectric voltage V_{th} (or current) of the porous graphene foam increases with the temperature gradient ΔT (Fig. 2c, Supplementary Fig. 2) following a linear relationship with a slope representing the Seebeck coefficient S_T of 9.703 µV/°C (Fig. 2d). The generated thermoelectric voltage is still as high as ~6 µV for a small temperature gradient ΔT of 0.5 °C (Fig. 2e), allowing it to harvest low-grade environmental heat and sensitively detect the temperature variations. The generated thermoelectric voltage directed from the low- to high-temperature end due to electron diffusion from the hot to cold end (driven by the temperature differential) is consistent with the n-type thermoelectric graphene[57]. It is worth noting that the variations in the initial resistance (1.3–1.2 kΩ with a rate of change of 7.7%) and Seebeck coefficient S_T (9.7 to 8.9 µV/°C with a rate of change of 8.2%) of the sensor in the environmental temperature range from 10 to 100°C are negligible (Supplementary Fig. 3). Reliable experimental measurements in this study are obtained from five sensors with five measurements from each sensor (to provide the average value and standard deviation represented as the error bars). As the tensile strain increases from 0 to 45%, the almost linear I–V curves with increased resistance and decreased slope still exhibit Ohmic behavior (Fig. 2f). The porous graphene foam also shows highly repeatable (Fig. 2g) and sensitive response (Fig. 2h) to the applied tensile strain from 5 to 45%. While relatively small tensile strain leads to deformation and rotation of porous graphene, large stretching generates microcracks to induce significant resistance changes, resulting in increased gauge factor upon stretching as in the previous literature reports[58–60]. The piecewise linear calibration curve shows a reasonably high gauge factor defined as the ratio of normalized resistance change to the strain ($\Delta R/R_O$)/ε: 109.8 in 0–30% and 1401.5 in 30–45%. Besides the high sensitivity, the sensor can also detect subtle strain variations of 0.05, 0.1, 0.2, 0.4, and 0.8% (Fig. 2i).

Decoupled sensing of temperature gradient and strain based on the porous graphene foam

The independent measurements of thermoelectric voltage and resistance allow the simultaneous detection of temperature and strain. In fact, the I-V curves follow $R(\epsilon)I = V + V_{th}(\Delta T)$, where R is the resistance due to the strain only. The strain input has a vanishing effect on the generated thermoelectric voltage $\left(\frac{\partial V_{th}}{\partial \epsilon} \approx 0\right)$, and the temperature stimuli have a negligible effect on the electrical resistance $\left(\frac{\partial R}{\partial T} \approx 0\right)$. As a result, temperature and strain stimuli can be decoupled by using the measured thermoelectric voltage and electrical resistance, respectively.

The well-separated I–V curves of the stretchable thermoelectric sensor based on the porous graphene foam measured at varied temperature gradients ΔT (0, 3, 6, 9, and 12 °C) and tensile strain levels (5% and 15%) demonstrate the decoupled sensing of temperature and strain (Fig. 3a). The generated thermoelectric voltages are determined by the temperature gradient without being affected by the varied strain levels (Fig. 3b, c). Meanwhile, the electrical resistance (or the inverse of the slope of the I–V curve) is only affected by the strain (Fig. 3a, d).

The cyclic response and the corresponding calibration curve of the relative electrical resistance versus strain from 15–45% at a temperature gradient of 6 °C (with a thermoelectric voltage of 58 mV) (Supplementary Fig. 5a, b) are almost identical to those from the sensor driven by an extra power supply (Fig. 2g). This result implies the potential use of the device for self-powered sensing. This negligibly small effect is also observed for the sensor to detect subtle strains
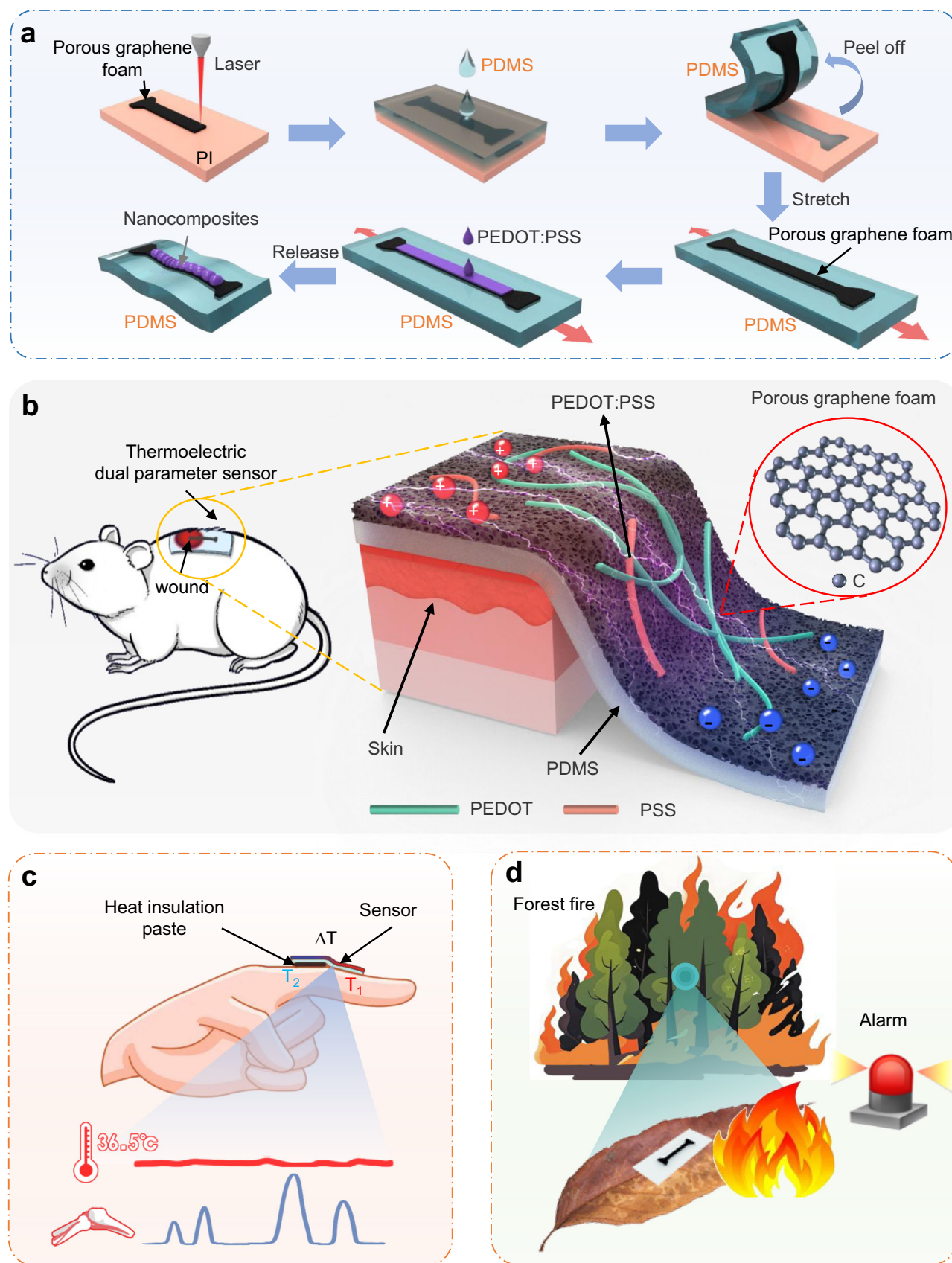
Fig. 1 | Overall design and application of the thermoelectric porous laser-induced graphene nanocomposites. a Fabrication, (**b**) structure, and application of the self-powered sensors based on porous graphene foams for decoupled detection of temperature and strain for (**c**) in situ wound healing monitoring in mice and (**d**) remote fire alarm warning. PDMS: polydimethylsiloxane, PI: polyimide, PEDOT:PSS: poly (3,4-ethylenedioxythiophene)/poly (styrenesulfonate).
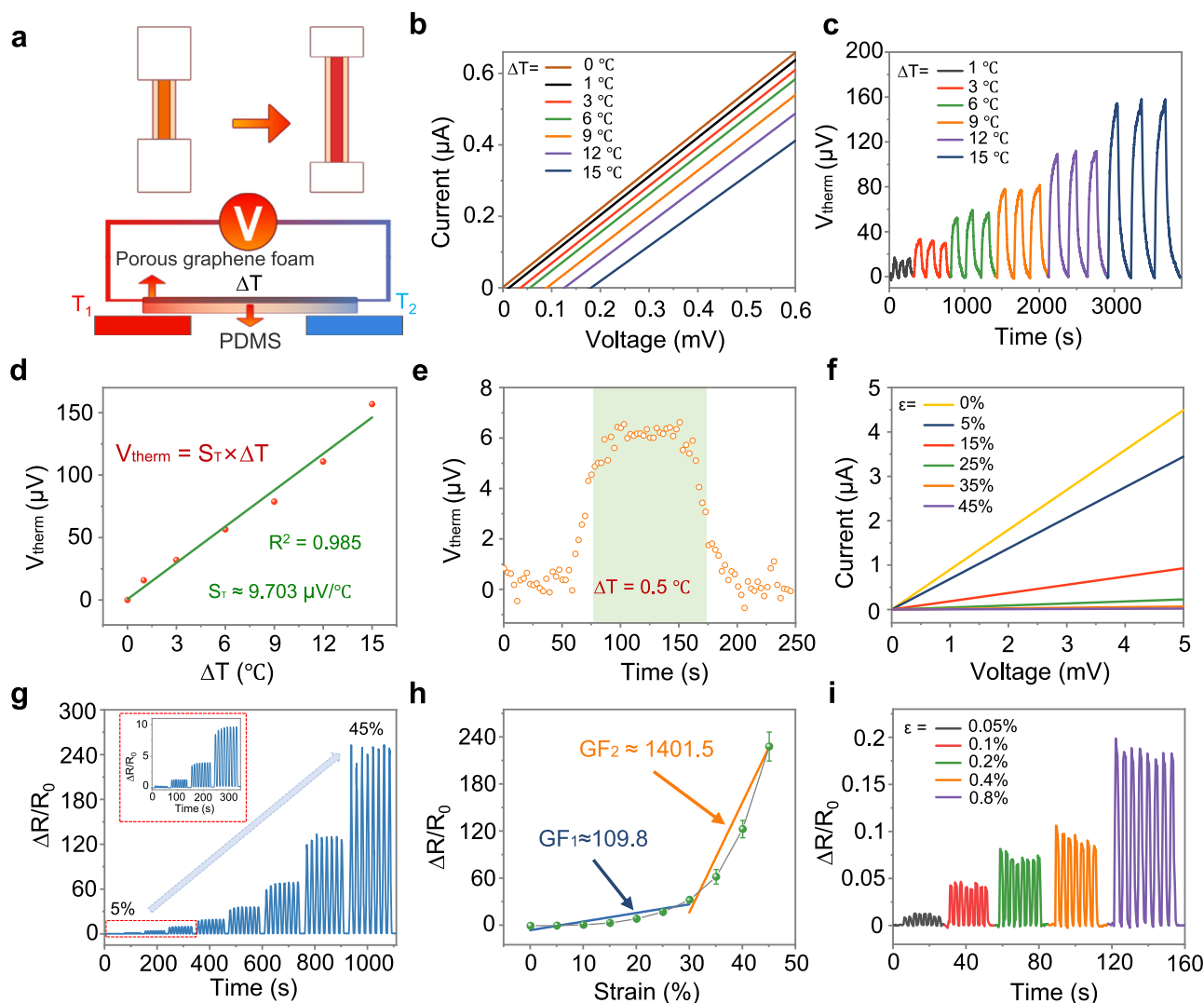
Fig. 2 | Characterization of the porous graphene foam in response to the temperature gradient and tensile strain. a Schematic showing the experimental setup for the measurements ($\Delta T = T_1 \cdot T_2$). **b** I–V curves of the sensor in response to a thermal gradient $\Delta T = 0, 1, 3, 6, 9,$ and 15 °C. **c** The change in the thermoelectric voltage with ΔT in the range from 1 to 15 °C and its (**d**) linear fit to determine the Seebeck coefficient. **e** Output response signal of a device to a biased minimum temperature gradient of 0.5 °C. **f** I–V curves of the sensor in response to tensile strain from 0 to 45%. Relative resistance variation as a function of (**g**) time and (**h**) strain for a tensile strain in the range of 5 to 45%, with the gauge factor (GF) labeled in the plot. The standard deviation (SD) is shown as error bars ($n = 3$). **i** Relative resistance variation of the sensor under subtle strain levels of 0.05, 0.1, 0.2, 0.4, and 0.8%.

(0.1%, 0.2%, 0.4%, and 0.8%) (ΔT of 3 °C) (Supplementary Fig. 5c). The normalized current changes from the sensor upon 10% stretching are ca. 67.2% across temperature gradients of 0, 3, 6, 9, and 12 °C (Fig. 3e, Supplementary Fig. 6). The output current decreases exponentially with increasing strain from 0% to 45% due to the increased resistance of the sensor after stretching (Fig. 3f), but the relationship between the natural logarithm of current output and the strain becomes linear (Fig. 3f, inset) with a slope of −0.0849 ln(nA)/%.

The strain-dependent relative resistance change $\Delta R/R_O$ and temperature-dependent thermoelectric voltage V_{th} (Fig. 4a) allow simultaneous and real-time sensing of the temperature gradient (0–6 °C) and strain (0–25%) (Fig. 4b). By placing a load with a resistance R_L of 100 Ω in series with the device, both voltages and currents of the load resistor are monitored (Supplementary Fig. 7). As the temperature gradient increases from 0 to 3 °C, the thermoelectric voltage V_{th} gradually increases from 0 (c-1) to 25 μV (c-2), with the same vanishing relative resistance change $\Delta R/R_O$ due to the strain of 0%. Subsequently increased temperature gradient to 6 °C and strain to 15% results in increased V_{th} to 55 μV and $\Delta R/R_O$ from 0 to 6 (c-3). Further

increasing the tensile strain to 25% while keeping the temperature gradient (at 6 °C) increases $\Delta R/R_O$ to 17.5 (c-4). Reducing the strain to 15% and temperature gradient to 3 °C gives V_{th} of 25 μV and $\Delta R/R_O$ of 6.5 (c-5). Further relaxing the applied strain to 0% and the temperature gradient to 0°C provides the vanishing readouts (c-6). The final readings at an applied strain of 0% are not exactly zero because of the drift in the initial resistance that results from the tiny changes in the ambient environment as in the previous literature reports[61,62]. In addition, the decoupled sensing experiments to simultaneously detect temperature gradient (from 0 to 60°C) and strain (from 0 to 40%) demonstrate the stable thermoelectrical property of the reported sensor over a large stain range in a large temperature variation (Supplementary Fig. 8).

Performance characterization of the porous graphene foam nanocomposite with PEDOT:PSS in response to temperature gradient and textile strain

The thermoelectric property of the intrinsic porous graphene foam can be further enhanced by forming a nanocomposite with
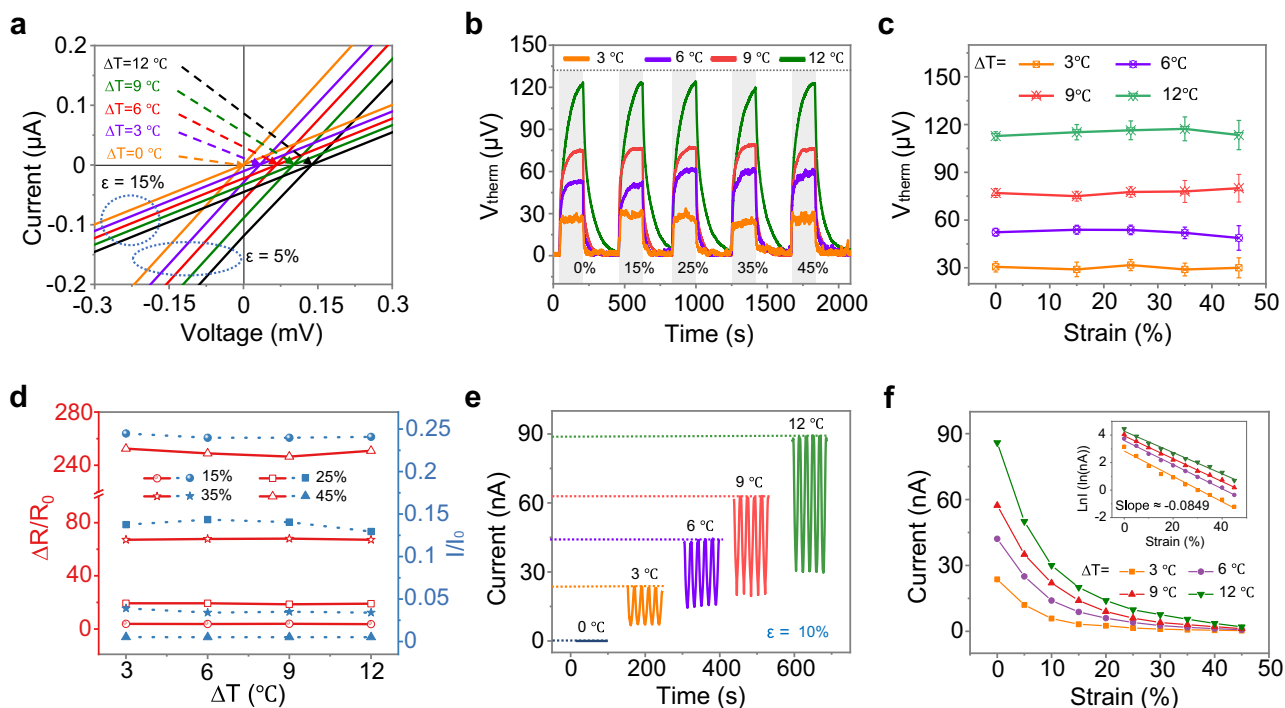
Fig. 3 | Decoupled sensing of simultaneously applied temperature gradient and strain with the stretchable thermoelectric sensor based on the porous graphene foam. **a** Measured *I–V* curves under different temperature gradients (0, 3, 6, 9, and 12 °C), and strain levels (5% and 15%). Thermoelectric voltage as a function of (**b**) time (strain of 0, 15, 25, 35, and 45%) and (**c**) strain for different temperature gradients (3, 6, 9, and 12 °C). The output voltage fluctuation at 3, 6, 9, and 12 °C is 9.1%, 9.8%, 6.5%, and 4.0% respectively, as the strain increases from 0% to 45%. The standard deviation (SD) is shown as error bars (*n* = 3). **d** Normalized relative resistance and current changes with the temperature gradient for different strain levels (15, 25, 35, and 45%). Thermoelectric current as a function of (**e**) time (10% stretching) and (**f**) strain for temperature gradients of 0, 3, 6, 9, and 12 °C, with log-linear fit shown in the inset.

PEDOT:PSS (Fig. 5a) through the pre-strain strategy (Fig. 1a). Filling the microcracked surface upon stretching with PEDOT:PSS (Supplementary Fig. 9) also increases the conductivity (Supplementary Fig. 10). The PEDOT:PSS is uniformly distributed in the layered structure (Supplementary Fig. 11), as evidenced by the uniform distribution of S (together with C and O) across the surface in the energy-dispersive X-ray spectroscopy (EDS) (Supplementary Fig. 12). The filling of the microcracks (dashed lines) with PEDOT:PSS is also supported by the higher content of the S element in these regions (marked by red circles in Supplementary Fig. 12d). The wide scan and S2p spectra in XPS show the broad peak between 166 and 172 eV of PSS (sulfonate moiety) from two spin-orbit splitting peak superpositions ($2p_{3/2}$ at 167.9 eV and $2p_{1/2}$ at 169.2 eV), and the band between 162 and 166 eV of PEDOT (thiophene ring) from the overlap of $2p_{3/2}$ at 163.9 eV and $2p_{1/2}$ at 165.1 eV (Fig. 5b and Supplementary Fig. 13). These results agree reasonably well with previously reported graphene/ PEDOT:PSS nanocomposites[63].

Compared with the intrinsic porous graphene foam, the nanocomposite with the PEDOT:PSS shows a significantly increased Seebeck coefficient from 9.703 to 37.33 µV/°C by 384.73% (Fig. 5c and Supplementary Fig. 14a) and improved temperature resolution from 0.5 to 0.2 °C (Supplementary Fig. 14b). However, the stretchability and sensitivity of the nanocomposite are slightly reduced due to the loss of the porous graphene textures (Fig. 5d and Supplementary Fig. 14c, d). Different from the bi-layered porous graphene/PDMS (Supplementary Fig. 1b), the tri-layered nanocomposite (Supplementary Fig. 11) with more mechanically mismatched interfaces exhibits declined stretchability and sensitivity. The stretchable nanocomposite shows almost unchanged sensing performance as the applied bias voltage reduces from 0.5 V to 5 µV (Fig. 5e), indicating drastically reduced energy consumption in the measurement circuit. The temperature gradient created by representative

everyday objects (e.g., alcohol, fingers, and hot water bottles) can be easily captured (Fig. 5f), in which endothermic reaction from the volatile alcohol produces a negative temperature gradient resulting in reverse voltage output. The nanocomposite that can decouple strain and temperature (Fig. 5g and Supplementary Fig. 15) allows real-time detection of human movement while harvesting the thermal energy (with a thermoelectric voltage of 100 µV for $\Delta T = 2.5$ °C between the finger and the environment) (Fig. 5h) for self-powered sensing. The sensors placed on five finger joints can also differentiate hand gestures for sign language detection to facilitate communication for people with language disorders (Supplementary Fig. 16). For instance, the expression "how are you" results in a vanishing strain signal from the thumb as in the fully relaxed state, along with large signals from the other four fingers in the second stage. With the index finger relaxed and the other four fingers bent in the third stage, the strain signal from the index finger vanishes as in the fully relaxed state, whereas the signals from the other four fingers exhibit large values. Creating a device array in series or parallel connection can also linearly increase the thermoelectric voltage (from 100 to 500 µV for five elements) (Fig. 5i) or current (from 75 to 375 nA for five elements) (Supplementary Fig. 17).

Self-powered decoupled sensing of temperature and strain for alerting fire

The thermoelectric voltage of the sensor based on the nanocomposite gradually increases as the distance to the fire source is decreased from 3 cm to 0.2 cm (for the same duration of 2 s) (Fig. 6a). When the distance to the fire source remains at 0.2 cm, the thermoelectric voltage also gradually increases with the increasing duration from 0.1 s to 2.5 s (Fig. 6b) and then saturates at a dwell time of 4 s, which is also true for the other distances (i.e., 3, 2, and 1 cm) (Supplementary Fig. 18). The immediate voltage increase that exceeds the defined threshold from
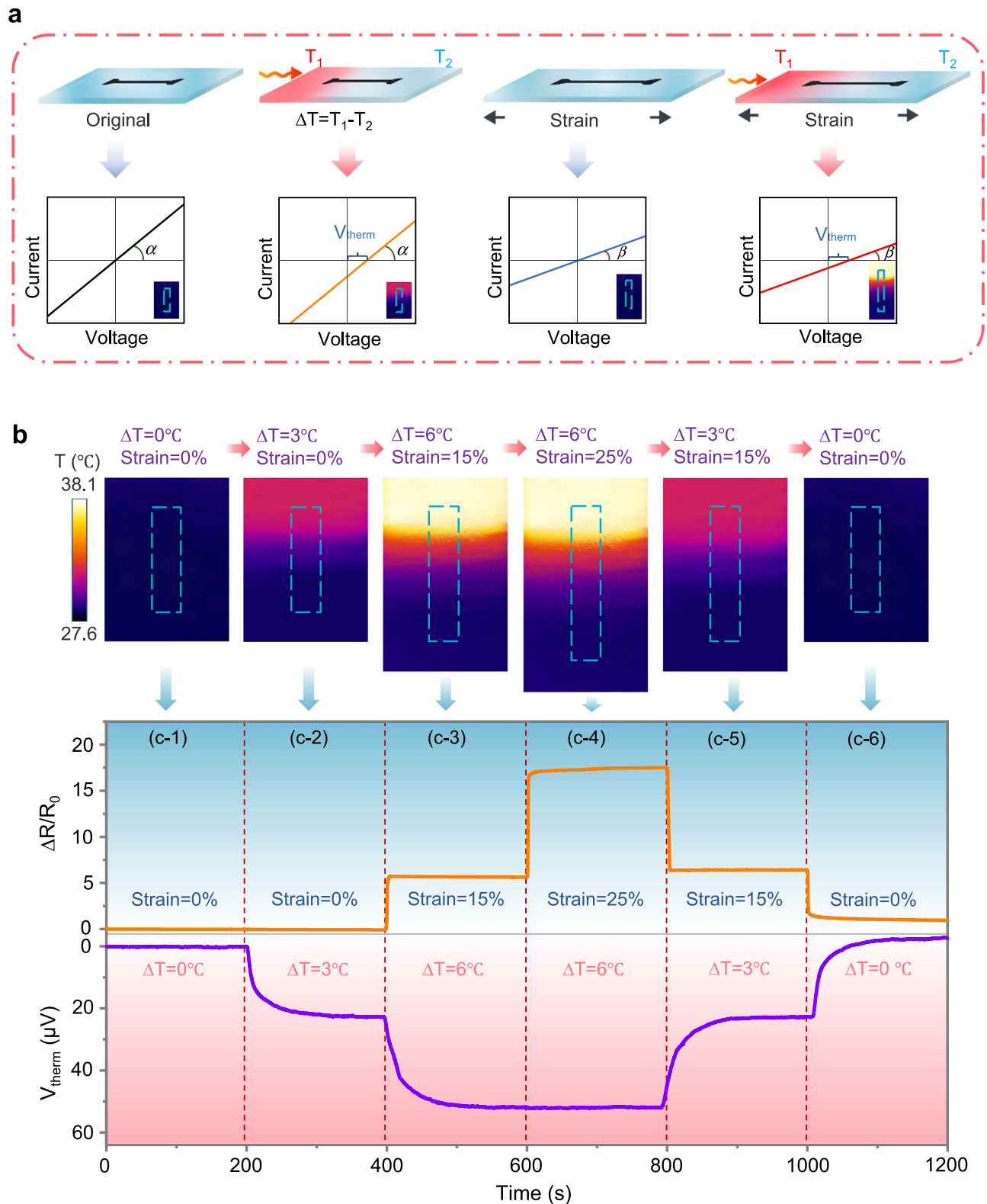
Fig. 4 | Decoupled sensing of temperature and strain. a Schematic and (**b**) demonstration of temperature-strain decoupling, with infrared thermal images of the device shown in the inset (temperature gradient from 0 to 6 °C and strain from 0 to 25%).

the fire can be processed by the backend device to trigger the red light and sound an alarm (or other warnings) in the alarm system (Fig. 6c). As a result, the device system can easily detect abnormal temperature increases (Fig. 6d) and simulated laboratory and forest fires (Fig. 6e and Supplementary Fig. 19).

Self-powered decoupled sensing of temperature and strain for monitoring in situ wound healing status

Highly accurate measurements of strain and temperature from decoupled sensing are vital to evaluate complicated biophysical processes such as skin wound healing that involves cell migration,
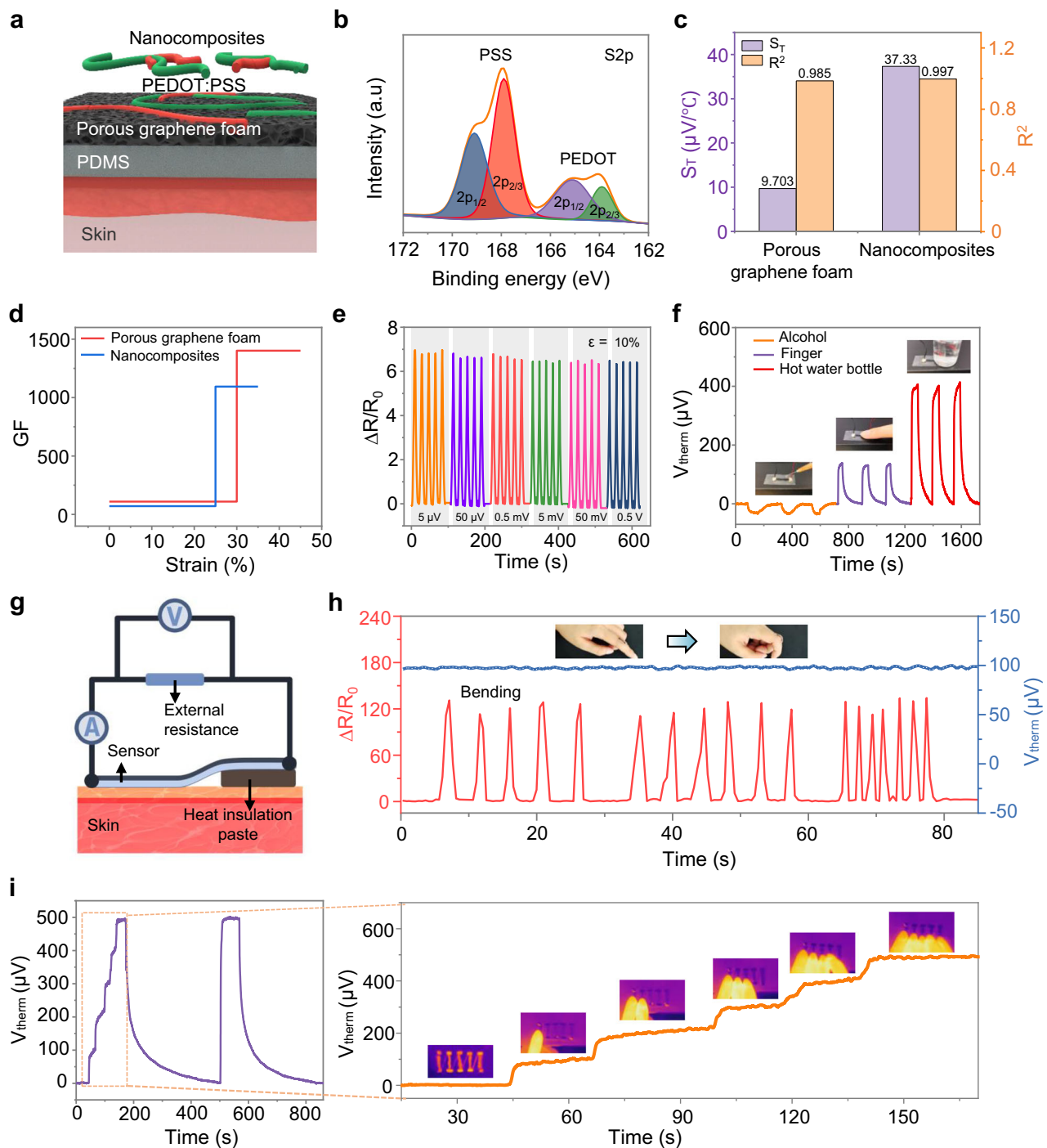
Fig. 5 | Design and demonstration of porous graphene foam nanocomposite with PEDOT:PSS. a Structure diagram of the stretchable thermoelectric sensor based on the nanocomposites. **b** XPS S2p spectrum of the nanocomposites. Performance in **c** Seebeck coefficient and **d** strain sensitivity of the nanocomposite (compared with the intrinsic porous graphene foam). **e** Effect of the biased voltage on strain sensing. **f** The thermoelectric voltage in response to alcohol, finger, and hot water bottle. **g** Schematic and **h** demonstration of the nanocomposite on the finger to detect motion while harvesting thermal energy. **i** Demonstration of the sensor array connected in series to linearly increase the output voltage.

proliferation, and natural tissue remodeling[64,65]. The temperature rise at the wound site may alert for inflammation, infection, and possible development into a chronic wound[66–69]. While the presence of tensile stress facilitates the growth of new blood vessels and cells, excessive stress would tear the newly grown tissue[70]. As a proof-of-the-concept demonstration, the sensor with decoupled sensing capability is applied on the back of the mice (Kunming model for high rates of reproduction/survival, low cost, and good resistance to illness) (Fig. 7a). In the pilot study with two Kunming

mice, two circular full-thickness wounds with a diameter of 10 mm symmetrically created on the back of each mouse provide the left one as the experimental group and the right other as the control group (Fig. 7b). The sensor on the left wound does not change the wound healing in terms of the wound closure rate (Fig. 7c) and status (Fig. 7d), when compared with the control group on the right wound. Besides excellent biocompatibility, the sensor can provide accurate measurements of the strain and temperature over the entire course of the wound healing process (taken for 10 min every
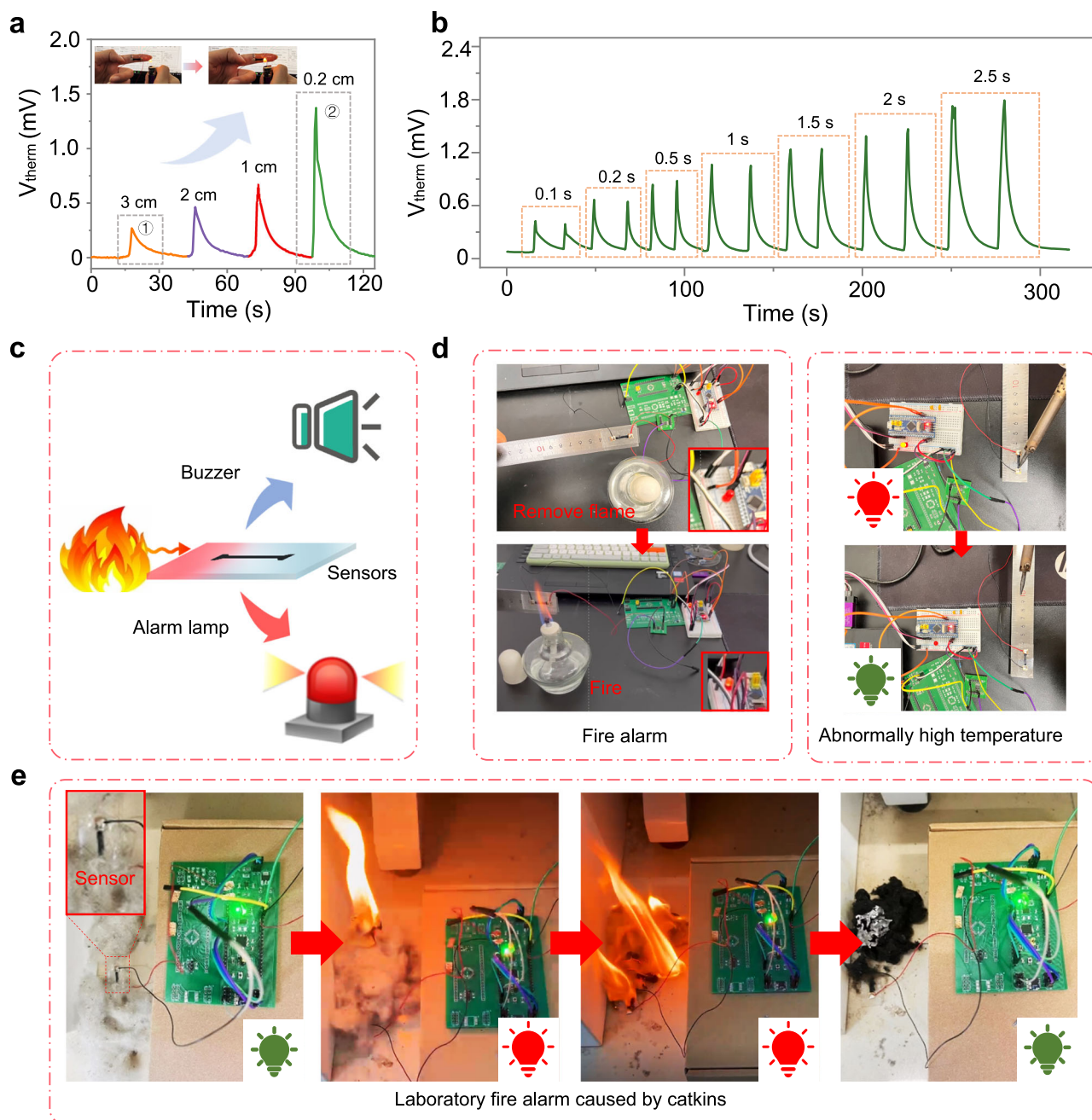
Fig. 6 | A smart fire alarm system based on thermoelectric nanocomposites. Detection of the fire source (**a**) positioned at different positions (3–0.2 cm) and (**b**) with different durations (0.1–2.5 s). **c** Schematic showing the structure of the fire alarm system and its demonstration to detect (**d**) fire and high temperature, as well as simulated (**e**) laboratory fires.

three days during anesthetization) (Fig. 7e). The wound temperature obtained from the temperature differential between the wound and the shaved skin on the first day after surgery (~37.7°C that is higher than the skin temperature of 36.4°C on other parts of the body) is attributed to inflammation that results from the migration of white blood cells to the wound site. Subsequently, the temperature starts to decrease due to healing and gradually diminished inflammation in the falling phase (1–9 days), which is followed by the plateau phase that is associated with a steady temperature change (36–36.5°C) for expedited recovery from cleared wound inflammation. The gradually reduced strain from 12% to 0% over 24 days also indicates the successful and complete healing of the wound (Fig. 7e).

Discussion

In conclusion, this work reports the design and demonstration of stretchable thermoelectric porous graphene foams for decoupled sensing of temperature and strain. The resulting sensor based on the intrinsic porous graphene foams exhibits a Seebeck coefficient of 9.703 μV/°C, temperature resolution of 0.5 °C, and high gauge factor of up to 1401.5. Introducing the PEDOT:PSS through a pre-strain strategy creates the stretchable foam nanocomposites with a Seebeck coefficient enhanced by almost four times while minimally affecting the other sensing parameters. The application of the device in self-powered sensing and fire alarm warning, as well as decoupled sensing of strain and temperature during the wound healing process in vivo on mice, provides a system-level
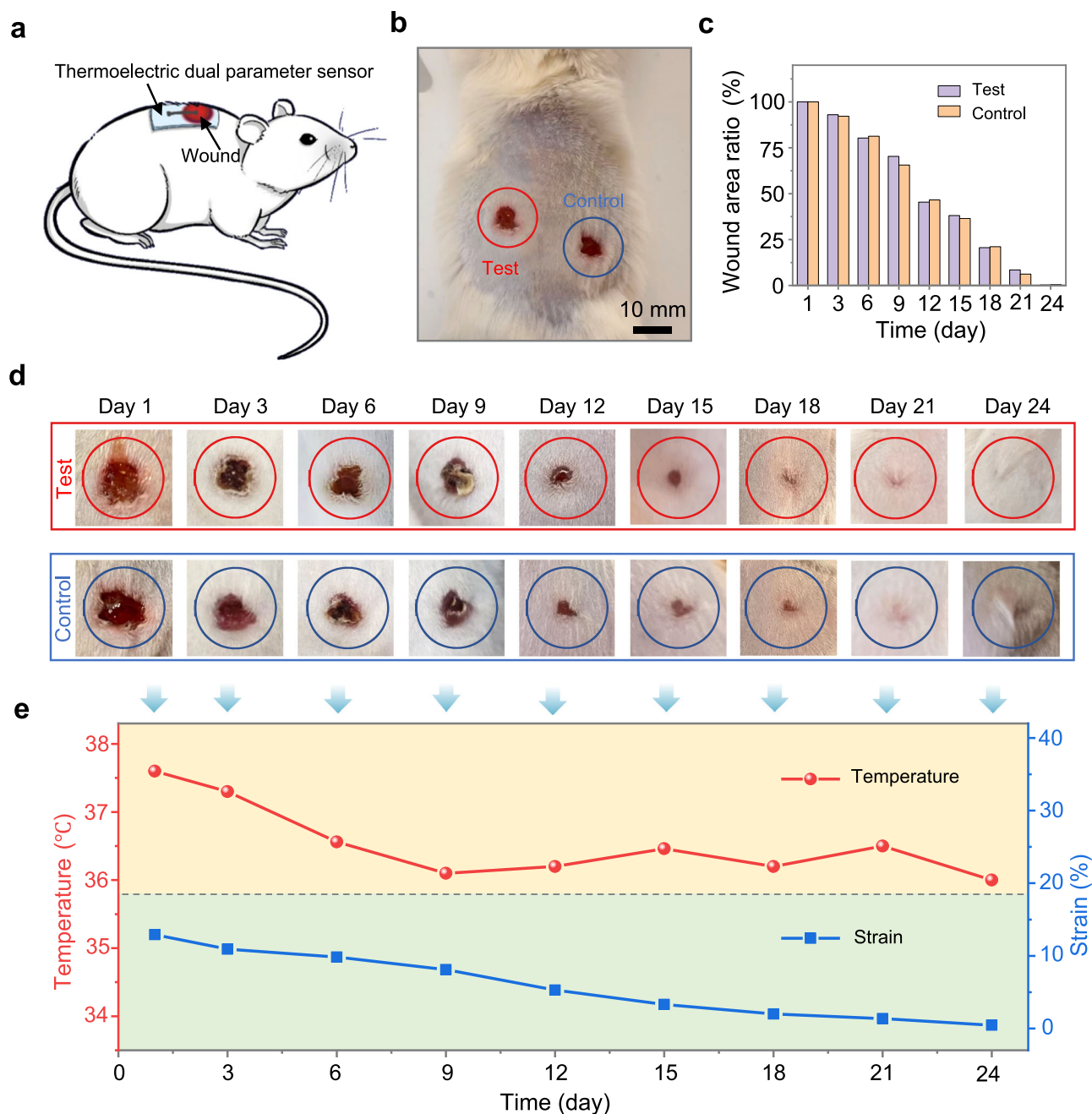
Fig. 7 | Application of the sensor to decouple temperature and strain over the wound healing process on mice. a Schematic and (**b**) digital image of surgical wounds on the back of mice with the left for experimental (dashed red) and right for control (dashed blue) groups. Comparison in wound closure in terms of (**c**) wound area and (**d**) optical images between the experimental and control groups after 1, 3, 6, 9, 12, 15, 18, 21, and 24 days. **e** Measured temperature and strain changes over the course of 24 days.

demonstration and opens up opportunities for future self-powered decoupled multimodal sensors.

Methods

Materials

Polyimide (PI) film with a thickness of 75 μm was purchased from Suzhou Dongxuan Plastic Products Co. Ltd (Jiangsu, China). The water-soluble tape was obtained from the Yongri adhesive Co. Ltd. (Shanghai, China). The PDMS Kit (Sylgard 184 Silicone Elastomer) was purchased from Dow Corning Corporation (U.S.A.). The PEDOT:PSS conductive coating solution (S315-1%) was purchased from Zhuhai Kaiwei Optoelectronics Technology Co., Ltd. (Guangdong, China).

Fabrication of the porous graphene foams and their nanocomposites on PDMS

After creating the computer-designed layout, the 3D porous graphene foam in the dog bone shape with a length of 15 mm and a width of 1.2 mm was rapidly fabricated on a commercial Kapton PI film in the ambient environment by using a CO_2 infrared laser (wavelength ~ 10.6 μm, power ~ 12 W, scanning speed ~ 508 mm s⁻¹, Universal Laser System). Uniformly coating and curing (at 100 °C for 40 min) 1 mL of PDMS precursor solution with a 10:1 (prepolymer A: crosslinker B) weight ratio on the sensor area was followed by peeling to prepare the porous graphene foam on PDMS. After pre-stretching the porous graphene foam/PDMS film by 50% and fixing it on the glass plate with two clips, the PEDOT:PSS solution was coated by the doctor blade

technique, followed by drying at 35 °C for 15 min. The release of the pre-strain yielded the nanocomposites on PDMS. An aluminum foil mounted at the two ends of the sample served as an electrical connection to the data acquisition system for measurements.

Monitoring of physiological signs during the wound-healing process

Male Kunming mice weighing 22 ± 3 g were procured from Beijing Huafukang Biotechnology Co., Ltd. All animal subject studies were approved by the Biomedical Ethics Committee of the Hebei University of Technology (protocol number HEBUTacvc2023045). The full-layer skin defect wound model on mice was created for simultaneous monitoring of temperature and strain throughout the wound healing process by the dual-mode sensors. To avoid discomfort and slowdown of the wound healing process during frequent daily activities, the sensor was only applied to the wound during each test (and removed after the test). Specifically, the temperature-strain decoupled sensor was applied to measure the temperature and strain from the wounds on the 1st, 3rd, 6th, 9th, 12th, 15th, 18th, 21st, and 24th days post-surgery, with images of the wounds captured by a digital camera. On the first day post-surgery, the mice were intraperitoneally anesthetized with 10% chloral hydrate, with the skin and sensors sterilized with 75% ethanol. The monitoring was approximately 10 minutes and then the sensors were removed with the placement locations marked on the mice. On the following days of measurements, the same anesthesia and sensor sterilization procedures were followed before attaching the sensors to the marked positions.

Characterization and measurements

The scanning electron microscope (SEM, Nova Nano SEM450), energy dispersive spectrometry (EDS, OCTANE PLUS), and X-ray photoelectron spectroscopy (XPS, ESCALAB 250Xi) were used to analyze the morphology and composition of the porous graphene foams and nanocomposites. Thermoelectric and sensing performance was evaluated by using Peltier elements (20×20 mm), force gauge (JSV-H1000 and HF-1), and source meter (Keithley 2400). All human subject studies were approved by the Institutional Review Board of the Hebei University of Technology and the volunteers gave informed consent.

Reporting summary

Further information on research design is available in the Nature Portfolio Reporting Summary linked to this article.

Data availability

All the data supporting the findings of this study are available within this paper and its Supplementary Information. Any additional information can be obtained from the corresponding author on request.

References

1. Yang, L. et al. Intrinsically breathable and flexible NO_2 gas sensors produced by laser direct writing of self-assembled block copolymers. *ACS Appl. Mater. Interfaces* **14**, 17818–17825 (2022).
2. Xue, Y. et al. Superhydrophobic, stretchable kirigami pencil-on-paper multifunctional device platform. *Chem. Eng. J.* **465**, 142774 (2023).
3. Yang, H. et al. Topographic design in wearable MXene sensors with in-sensor machine learning for full-body avatar reconstruction. *Nat. Commun.* **13**, 5311 (2022).
4. Sempionatto, J. R. et al. An epidermal patch for the simultaneous monitoring of haemodynamic and metabolic biomarkers. *Nat. Biomed. Eng.* **5**, 737–748 (2021).
5. Yang, L. et al. Self-healing, reconfigurable, thermal-switching, transformative electronics for health monitoring. *Adv. Mater.* **35**, 2207742 (2023).
6. Wu, Z. et al. A humidity-resistant, sensitive, and stretchable hydrogel-based oxygen sensor for wireless health and environmental monitoring. *Adv. Funct. Mater.* **34**, 2308280 (2023).
7. Yang, L. et al. Wearable pressure sensors based on MXene/tissue papers for wireless human health monitoring. *ACS Appl. Mater. Interfaces* **13**, 60531–60543 (2021).
8. Chen, X. et al. A laser-scribed wearable strain sensing system powered by an integrated rechargeable thin-film zinc-air battery for a long-time continuous healthcare monitoring. *Nano Energy* **101** (2022).
9. Yang, L. et al. Novel gas sensing platform based on a stretchable laser-induced graphene pattern with self-heating capabilities. *J. Mater. Chem. A* **8**, 6487–6500 (2020).
10. Yang, L. et al. Moisture-resistant, stretchable NO_X gas sensors based on laser-induced graphene for environmental monitoring and breath analysis. *Microsyst. Nanoeng.* **8**, 78 (2022).
11. Niu, G. et al. Pencil-on-paper humidity sensor treated with NaCl solution for health monitoring and skin characterization. *Nano Lett.* **23**, 1252–1260 (2023).
12. Lu, Y. et al. Stretchable graphene-hydrogel interfaces for wearable and implantable bioelectronics. *Nat. Electron.* **7**, 51–65 (2024).
13. Wang, H. et al. High-performance hydrogel sensors enabled multimodal and accurate human-machine interaction system for active rehabilitation. *Adv Mater.* **36**, e2309868 (2023).
14. Wang, Z. et al. Conformal in-ear bioelectronics for visual and auditory brain-computer interfaces. *Nat. Commun.* **14** (2023).
15. Lu, Y. et al. Machine learning-enabled tactile sensor design for dynamic touch decoding. *Adv. Sci.* **10**, 2303949 (2023).
16. Hong, S. Y. et al. Intrinsically stretchable and printable lithium-ion battery for free-form configuration. *ACS Nano* **16**, 2271–2281 (2022).
17. Zhao, X. F. et al. Spider web-like flexible tactile sensor for pressure-strain simultaneous detection. *ACS Appl. Mater. Interfaces* **13**, 10428–10436 (2021).
18. Zhang, Y. et al. Flexible self-powered integrated sensing system with 3D periodic ordered black phosphorus@MXene thin-films. *Adv. Mater.* **33**, 2007890 (2021).
19. Park, H. et al. Dynamically stretchable supercapacitor for powering an integrated biosensor in an all-in-one textile system. *ACS Nano* **13**, 10469–10480 (2019).
20. Xu, H. et al. A fully integrated, standalone stretchable device platform with in-sensor adaptive machine learning for rehabilitation. *Nat. Commun.* **14**, 7769 (2023).
21. Zhang, J. et al. Finger-inspired rigid-soft hybrid tactile sensor with superior sensitivity at high frequency. *Nat. Commun.* **13**, 5076 (2022).
22. Lin, Y. et al. Printable fabrication of a fully integrated and self-powered sensor system on plastic substrates. *Adv. Mater.* **31**, 1804285 (2019).
23. Wang, X. et al. Specific and long-term luminescent monitoring of hydrogen peroxide in tumor metastasis. *Adv. Mater.* **35**, 2210948 (2023).
24. Yan, Z. et al. Flexible high-resolution triboelectric sensor array based on patterned laser-induced graphene for self-powered real-time tactile sensing. *Adv. Funct. Mater.* **31**, 2100709 (2021).
25. Deng, H. T. et al. Super-stretchable multi-sensing triboelectric nanogenerator based on liquid conductive composite. *Nano Energy* **83**, 105823 (2021).
26. Zhao, Z. et al. Rationally patterned electrode of direct-current triboelectric nanogenerators for ultrahigh effective surface charge density. *Nat. Commun.* **11**, 6186 (2020).
27. Xia, X. et al. Metallic glass-based triboelectric nanogenerators. *Nat. Commun.* **14**, 1023 (2023).
28. Luo, H. et al. A fully soft, self-powered vibration sensor by laser direct writing. *Nano Energy* **103**, 107803 (2022).

29. Xu, S. et al. Highly flexible, stretchable, and self-powered strain-temperature dual sensor based on free-standing PEDOT:PSS/carbon nanocoils-poly(vinyl) alcohol films. *ACS Sens.* **6**, 1120–1128 (2021).

30. Liu, Y. et al. Scalable-produced 3D elastic thermoelectric network for body heat harvesting. *Nat. Commun.* **14**, 3058 (2023).

31. Chi, C. et al. Reversible bipolar thermopower of ionic thermoelectric polymer composite for cyclic energy generation. *Nat. Commun.* **14**, 306 (2023).

32. Zhu, M. et al. Self-powered and self-functional cotton sock using piezoelectric and triboelectric hybrid mechanism for healthcare and sports monitoring. *ACS Nano* **13**, 1940–1952 (2019).

33. Huang, Z. X. et al. Self-poled piezoelectric polymer composites via melt-state energy implantation. *Nat. Commun.* **15**, 819 (2024).

34. Vinikoor, T. et al. Injectable and biodegradable piezoelectric hydrogel for osteoarthritis treatment. *Nat. Commun.* **14**, 6257 (2023).

35. Xu, C. et al. Portable and wearable self-powered systems based on emerging energy harvesting technology. *Microsyst. Nanoeng.* **7**, 25 (2021).

36. Bariya, M. et al. Wearable sweat sensors. *Nat. Electron.* **1**, 160–171 (2018).

37. Liang, J. et al. Modulation of the morphotropic phase boundary for high-performance ductile thermoelectric materials. *Nat. Commun.* **14**, 8442 (2023).

38. Wan, K. et al. Highly stretchable and sensitive self-powered sensors based on the N-Type thermoelectric effect of polyurethane/Nax(Niett)n/graphene oxide composites. *Compos. Commun.* **28**, 100952 (2021).

39. Akbar, Z. et al. Intrinsically self-healable, stretchable thermoelectric materials with a large ionic Seebeck effect. *Energy Environ. Sci.* **13**, 2915–2923 (2020).

40. Heo, S. H. et al. Solution-processed hole-doped SnSe thermoelectric thin-film devices for low-temperature power generation. *ACS Energy Lett.* **7**, 2092–2101 (2022).

41. Jia, Y. et al. Wearable thermoelectric materials and devices for self-powered electronic systems. *Adv. Mater.* **33**, 2102990 (2021).

42. Jang, D. et al. Highly stretchable three-dimensional thermoelectric fabrics exploiting woven structure deformability and passivation-induced fiber elasticity. *Nano Energy* **97**, 107143 (2022).

43. Zhu, P. et al. Recyclable, healable, and stretchable high-power thermoelectric generator. *Adv. Energy Mater.* **11**, 2100920 (2021).

44. Sun, T. et al. Stretchable fabric generates electric power from woven thermoelectric fibers. *Nat. Commun.* **11**, 572 (2020).

45. Yu, H. et al. Flexible temperature-pressure dual sensor based on 3D spiral thermoelectric Bi_2Te_3 films. *Nat. Commun.* **15**, 2521 (2024).

46. Lee, B. et al. High-performance compliant thermoelectric generators with magnetically self-assembled soft heat conductors for self-powered wearable electronics. *Nat. Commun.* **11**, 5948 (2020).

47. Xu, K. et al. Laser direct writing of flexible thermal flow sensors. *Nano Lett.* **23**, 10317–10325 (2023).

48. Chen, X. et al. Porous graphene foam composite-based dual-mode sensors for underwater temperature and subtle motion detection. *Chem. Eng. J.* **444**, 136631 (2022).

49. Yang, L. et al. Vanadium oxide-doped laser-induced graphene multi-parameter sensor to decouple soil nitrogen loss and temperature. *Adv. Mater.* **35**, 2210322 (2023).

50. Yang, L. et al. Fully stretchable, porous MXene-graphene foam nanocomposites for energy harvesting and self-powered sensing. *Nano Energy* **103**, 107807 (2022).

51. Zhang, F. et al. Flexible and self-powered temperature-pressure dual-parameter sensors using microstructure-frame-supported organic thermoelectric materials. *Nat. Commun.* **6**, 8356 (2015).

52. Yang, R. et al. Multimodal sensors with decoupled sensing mechanisms. *Adv. Sci.* **9**, 2202470 (2022).

53. Rao, J. et al. Tactile electronic skin to simultaneously detect and distinguish between temperature and pressure based on a tribo-electric nanogenerator. *Nano Energy* **75**, 105073 (2020).

54. Qiu, Y. et al. Bioinspired, multifunctional dual-mode pressure sensors as electronic skin for decoding complex loading processes and human motions. *Nano Energy* **78**, 105337 (2020).

55. Gao, F. L. et al. $Ti_3C_2T_x$ MXene-based multifunctional tactile sensors for precisely detecting and distinguishing temperature and pressure stimuli. *ACS Nano* **17**, 16036–16047 (2023).

56. Lin, J. et al. Laser-induced porous graphene films from commercial polymers. *Nat. Commun.* **5**, 5714 (2014).

57. Chen, M. et al. Ionic liquid gating enhanced photothermoelectric conversion in three-dimensional microporous graphene. *ACS Appl. Mater. Interfaces* **12**, 28510–28519 (2020).

58. Wang, W. et al. Fingerprint-inspired strain sensor with balanced sensitivity and strain range using laser-induced graphene. *ACS Appl. Mater. Interfaces* **14**, 1315–1325 (2021).

59. Yu, T. et al. High electrical self-healing flexible strain sensor based on MWCNT- polydimethylsiloxane elastomer with high gauge factor and wide measurement range. *Compos. Sci. Technol.* **238**, 110049 (2023).

60. Luo, Y. et al. Heterogeneous strain distribution based programmable gated microchannel for ultrasensitive and stable strain sensing. *Adv. Mater.* **35**, 2207141 (2022).

61. Wang, C. et al. Carbonized silk georgette as an ultrasensitive wearable strain sensor for full-range human activity monitoring. *J. Mater. Chem. C* **5**, 7604–7611 (2017).

62. Wang, S. et al. Network cracks-based wearable strain sensors for subtle and large strain detection of human motions. *J. Mater. Chem. C* **6**, 5140–5147 (2018).

63. Wang, X. et al. An effective dual-solvent treatment for improving the thermoelectric property of PEDOT:PSS with white graphene. *J. Mater. Sci.* **52**, 9806–9818 (2017).

64. Xiao, X. et al. Triboelectric nanogenerators for self-powered wound healing. *Adv. Healthc. Mater.* **10**, 2100975 (2021).

65. Long, Y. et al. Effective wound healing enabled by discrete alternative electric fields from wearable nanogenerators. *ACS Nano* **12**, 12533–12540 (2018).

66. Zhu, J. et al. Smart bioadhesives for wound healing and closure. *Bioact. Mater.* **19**, 360–375 (2023).

67. Zeng, Q. et al. Wound dressing: from nanomaterials to diagnostic dressings and healing evaluations. *ACS Nano* **16**, 1708–1733 (2022).

68. Hwang, J. et al. Monitoring wound healing with topically applied optical nanoFlare mRNA nanosensors. *Adv. Sci.* **9**, 2104835 (2022).

69. Wang, L. et al. Multifunctional hydrogel as wound dressing for intelligent wound monitoring. *Chem. Eng. J.* **433**, 134625 (2022).

70. Jose, M. et al. Stretchable printed device for the simultaneous sensing of temperature and strain validated in a mouse wound healing model. *Sci. Rep.* **12**, 10138 (2022).

Acknowledgements

Author contributions

L. Yang: Contributed to the conception of the study and wrote the manuscript. X. Chen: Led the experiments of strain sensor and collected the overall data, co-wrote the draft of the manuscript. A. Dutta, H. Zhang,

Z Wang, M. Xin, S Du, and G. Xu: Performed the data analysis and co-wrote the paper. H Cheng: Contributed to the conception of the study and wrote the manuscript. All authors provided feedback on the manuscript.

Competing interests

L.Y. and H.C. are filing a provisional patent on this work. The remaining authors declare no competing interests.

Additional information

Supplementary information The online version contains supplementary material available at https://doi.org/10.1038/s41467-024-55790-x.

Correspondence and requests for materials should be addressed to Li Yang or Huanyu Cheng.

Peer review information *Nature Communications* thanks the anonymous reviewer(s) for their contribution to the peer review of this work. A peer review file is available.

Reprints and permissions information is available at http://www.nature.com/reprints